This article has been accepted for publication in a future issue of this journal, but has not been fully edited. Content may change prior to final publication. Citation information: DOI 10.1109/TNANO.2018.2849404, IEEE Transactions on Nanotechnology

Enhanced Non-Vector Space Approach for Nanoscale Motion Control

Bo Song, *Member, IEEE*, Zhiyong Sun, *Member, IEEE*, Ning Xi, *Fellow, IEEE*, Ruiguo Yang, *Member, IEEE*, Yu Cheng, *Student Member, IEEE*, Liangliang Chen, and Lixin Dong, *Senior Member, IEEE*

***Abstract*—Scanning probe microscopy (SPM) based nanomanipulators always experience probe accuracy issues caused by uncertainties such as scanner hysteresis, drifts, and interaction forces. Although some SPMs contain internal position sensors, they can hardly sense real probe position due to above uncertainties, especially when implementation scales down below 100 nm. Recently, we proposed a local-image-based non-vector space (NVS) control strategy for regulating nanomanipulator to enhance its accuracy (positioning error is generally maintained below 0.2% of the operation range). Since the previous NVS control strategy employs only local image and pixel-wise information (neglecting global location and local coherence information), it can hardly track trajectories with relatively large "jump" and heavy noise, which might be inefficient for practical implementation. To tackle these problems, this study proposes a novel enhanced NVS (ENVS) control strategy, which performs rough global positioning control through dynamic hysteresis compensation for SPM scanners to solve the "jump" problem; to realize fine positioning control with possible heavily noisy feedback, the ENVS controller utilizes patch-wise-based rather than pixel-wise-based set feedback strategy, and the ENVS is built based on a newly established shape Lyapunov function. Testing results show that the ENVS control scheme can precisely track references with jump changes, such as the step signal. Furthermore, the ENVS controller is able to maintain its accuracy even with extremely noisy feedback.**

I. Introduction

Imaging, manipulation, and measurement at nanoscale have revolutionized the nano world, which benefits the development and research of the biomedicine, material science, and physics [1]. As the centerpiece in nanotechnology, scanning probe microscopy (SPM) based nanomanipulators [2]–[5], have been widely used for various studies to manipulate and modify samples effectively, such as cellular-surgery [6], nanofabrication [7] and dynamical process observation [8]. The basic working principle of this kind of nanomanipulator is to control the 3D motion of the SPM probe to perform operation like robotic end-effector [9]. The operation accuracy of a nanomanipulator depends mainly on its motion control strategy, which is designed to control the output of the piezoelectric scanner to precisely locate its probe tip. Despite the piezoelectric scanner possesses various advantages such as fast response speed and nanometer spatial resolution, the nonlinearity (especially dynamic hysteresis) and uncertainties (such as thermal drift) [10]–[14] have been considered as major issues that significantly affect the tip motion accuracy. To reduce undesirable dynamic characteristics of scanners, typically, an SPM system is equipped with positioning sensors (such as capacitive sensor) to guarantee precise position control. However, these sensors have several drawbacks, such as bulky, costly, and sensitive to the environmental noise. Besides, the displacement measured by sensors is the output of the actuator, which is not the exact position of the probe tip since the cantilever of the probe is commonly bent due to different tip-sample interaction force during operation.

In order to design a control scheme to achieve accurate tip motion control without introducing extra positioning noise, recently, the SPM image feedback control method, named non-vector space (NVS) approach, has been proposed [15]. The NVS approach demonstrates that an image can be formatted and processed as a set inside this control scheme, and the images can be utilized as both the reference and the feedback to generate a closed-loop control system [16]. In the NVS control scheme, the image is generally considered as a set consisting of pixels (there is no order for each pixel in the set), and the controller is designed based on set dynamics, which guarantees motion accuracy even with local image varying [15]–[18].

Drawbacks of the NVS approach also exist. Previous studies on NVS control were mainly focused on deriving set dynamics and designing its stabilizing controller [16] based on merely the set dynamics and its pixel-wise information. However, in practice, current NVS scheme limits its performance in two dominant conditions: (1) Relatively large feedback image is required to cover possible positioning error caused by "jump" trajectory and actuator nonlinearity/uncertainty. (2) Under certain noisy situation, the NVS controller may converge to incorrect locations.

To maintain relatively small feedback set for each location, previous studies [15], [16] proposed the path planner method

B. Song is with Institute of Intelligent Machines, CAS, Hefei, 230031, China, and also with Department of Electrical and Computer Engineering, Michigan State University, East Lansing, MI, 48824, USA songbo@iim.ac.cn

Z. Sun and N. Xi are with Department of Industrial and Manufacturing Systems Engineering, The University of Hong Kong, Pokfulam, Hong Kong SAR {sunzy, xining}@hku.hk

R. Yang is with Department of Mechanical and Materials Engineering, University of Nebraska-Lincoln, Lincoln, NE, 68588 USA ryang6@unl.edu

Y. Cheng and L. Dong are with Department of Electrical and Computer Engineering, Michigan State University, East Lansing, MI, 48824, USA chengyu9@msu.edu, ldong@egr.msu.edu

L. Chen is with Shenzhen Academy of Robotics, Shenzhen, Guangdong, 230031, China, and also with Department of Electrical and Computer Engineering, Michigan State University, East Lansing, MI, 48824, USA chenlia5@msu.edu

This article has been accepted for publication in a future issue of this journal, but has not been fully edited. Content may change prior to final publication. Citation information: DOI 10.1109/TNANO.2018.2849404, IEEE Transactions on Nanotechnology

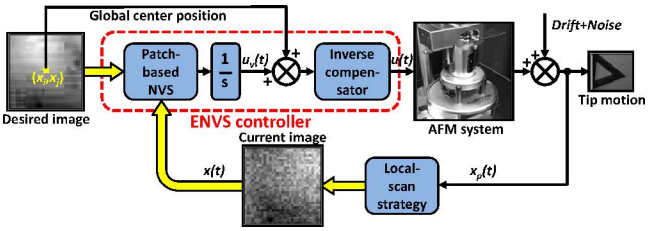

Fig. 1. Schematic diagram of the ENVS control scheme (with AFM as an instance).

to generate intermediate steps/positions to bridge the gap when the desired location is far away from current position for "jump" type trajectories. However, this method is still time-consuming and the requirement of bridging gap process is usually regarded as "cannot jump" limitation of the conventional NVS (CNVS) strategy.

To solve problems with CNVS approach for SPM nanomanipulation, an enhanced NVS (ENVS) control strategy is proposed in this study, which is comprised of a dynamic hysteresis compensator, an integral portion, and a novel patch-based-NVS control component (as shown in Fig. 1). The ENVS control strategy employs the dynamic hysteresis compensator to attenuate SPM actuator nonlinearity, therefore, it can reduce feedback image size and overcome the "cannot jump" limitation. In addition, the patch-based-NVS portion employs a new type shape Lyapunov function, which is based on patch-wise information, to enhance its discernibility under certain noisy situation.

To design such an ENVS control scheme, two crucial steps are involved: (1) Design a dynamic hysteresis compensator, which should be connected directly to the SPM scanner to linearize the actuator behavior. (2) Design a patch-based-NVS control strategy using newly developed shape Lyapunov function. The remaining contents of the paper are arranged as following: in section II, a dynamic hysteresis compensator is proposed for attenuating nonlinearity of the SPM scanner; section III presents the patch-wise-information-based NVS scheme design procedure, where a new shape Lyapunov function has been built; in section IV, comparative simulation tests on an AFM system are performed as specific examples to demonstrate the advantages of the ENVS controller in contrast to the CNVS approach; section V summarizes and concludes this study.

II. Dynamic Hysteresis Compensation for SPM Scanner

The scanner of SPM based manipulation systems is typically made by piezoelectric actuators with merits of high spatial resolution, fast response, and flexible structure [19], [20]. To design an ENVS controller, the first step is to build an inverse compensator to linearize nominal input-output relation of an SPM scanner. Cascaded with the inverse compensator, the original physical system can be altered into a highly linear virtual system to facilitate the ENVS controller design.

Piezoelectric materials usually possess dynamic hysteresis property as well as uncertainties such as thermal drift. Typically, their nominal input-output relation can be described utilizing a hysteresis-linear-dynamics cascade structure as shown in Fig. 2(a) [21], [22]. To efficiently compensate generalized dynamic hysteresis, precise and low-computation-cost compensator is desirable. To fulfill this aim, this study proposed a relatively simple generalized inverse compensator, which can be designed as two separate parts: the static hysteresis compensator and the linear dynamics compensator (as shown in Fig. 2(b)) [23].

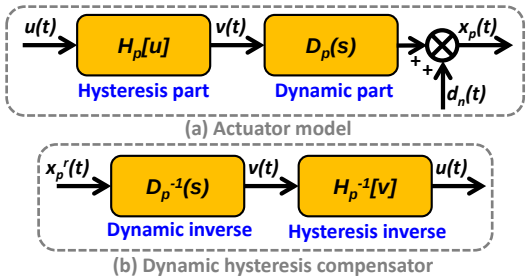

Fig. 2. Dynamic hysteresis modeling and compensation, (a) hysteresis-linear-dynamics cascade model, (b) nominal inverse compensator.

A. Static hysteresis compensator design

To conduct precise hysteresis compensation is difficult, as many types of complex hysteretic relation exist. To represent and then to reduce hysteretic effects accurately, lots of practical compensation approaches have been reported. Among them, operator based superposition models and compensation methods stand out for merits of flexible structures and supporting parallel computation which enhances efficiency. Typical operator based hysteresis model includes: Preisach model [24], Prandtl-Ishlinskii (PI) model [25], and its derivatives [21], [26], [27]. However, challenge still exists. Preisach model is universal for precisely compensating most hysteretic behavior [28]–[30], but it lacks efficiency in regard to computational cost [31]. Classical PI compensator is efficient, but can only handle symmetric hysteresis scenarios [25]. To tackle this issue, extensive efforts have been focused on asymmetric hysteresis modeling and compensation by adding or modifying memoryless functions [21], [26], [32], but for attenuating complex hysteresis they seem not accurate enough [33].

To accurately capture and then to reduce complex hysteresis of SPM scanners, in this study, the extended unparallel PI (E-UPI) model is employed, which generally guarantees modeling error below 2% for various types of hysteresis using around 20 hysteron, to directly model the inverse hysteretic relation considering its simplicity and accuracy [34]. The EUPI inverse is a superposition expression consisting of basic hysteron, UPI operator, described as (1),

$$\begin{aligned} &F_{r_i,\alpha_j}[v](t) \\ &\quad = \max\{v(t)-r_i,\ \min\{\alpha_j(v(t)+r_i), F_{r_i,\alpha_j}(t^-)\}\} \\ &\quad \text{with } t^- = \lim_{\delta\to 0^+}(t-\delta) \text{ and } r_i \geq 0,\ \alpha_j > 0, \end{aligned} \tag{1}$$

where $v(t)$ represents the drive signal at moment t; r_i denotes the i^{th} dead zone; and the slope of the UPI descending edge is regulated by the factor α_j.

This article has been accepted for publication in a future issue of this journal, but has not been fully edited. Content may change prior to final publication. Citation information: DOI 10.1109/TNANO.2018.2849404, IEEE Transactions on Nanotechnology

Typically, a complex hysteresis can be described utilizing two independent parts: memory and memoryless portion. For instance, the well-known Preisach model contains such a component comprised of all the zero-threshold operators. To establish a relatively sample inverse model while maintaining high precision, the polynomial function is employed as the memoryless part to combine with UPI operators to construct the inverse model, named EUPI inverse [34], as described in (2),

$$\begin{cases} H_p^{-1}[v](k) = \Gamma'_{UPI}[v](k) + P[v](k) \\ \Gamma'_{UPI}[v](k) = \sum_{i=1}^{N_r} \sum_{j=1}^{N_a} d'_{ij} F_{r_i,\alpha_j}[v](k) \\ P[v](k) = \sum_{i=1}^{N_p} p_i v^i(k) + p_0 \\ s.t.\ \alpha_j,\ r_i > 0,\ d'_{ij} \le 0, \end{cases} \tag{2}$$

where $H_p^{-1}[v](k)$ is the output of the EUPI inverse, $\Gamma'_{UPI}[v](k)$, and $P[v](k)$ are the memory and memoryless components, respectively; notation d'_{ij} and p_i are the weight gains for the corresponding UPI operators and memoryless part, respectively. N_p denotes the highest order of the polynomial function, and N_a and N_r are the total levels for the tilt α_j and the threshold r_i in the memory component. p_0 is a constant associated with the hysteresis initial condition. It is noted that all the weight gains d'_{ij} of the EUPI inverse are non-positive, therefore $\Gamma'_{UPI}[v](k)$ component is in the clockwise orientation.

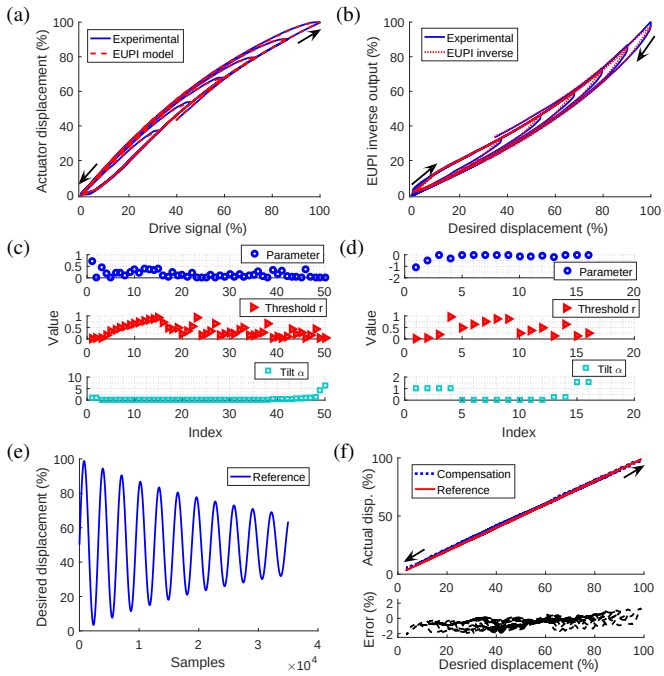

Fig. 3. Static complex hysteresis (normalized) compensation test using EUPI inverse, (a) forward input-output relation modeling using (2) of [34], (b) inverse input-output relation modeling, (c) parameters for the forward relation, (d) parameters for the inverse model, (e) input reference for static hysteresis compensation testing, (f) input-output relation after static hysteresis reduction, and the compensation error.

To demonstrate effectiveness of the EUPI inverse approach, the forward/inverse hysteresis modeling and compensation test was conducted based on normalized nano-positioning stage data. During the forward hysteresis modeling, the constrained least-squares (CLS) approach was employed, and N_r and N_a were predefined as 17 and 31, respectively, after several trials. After optimization, 50 UPI operator and a 3^{rd}-order polynomial function were determined, which can be found in Fig. 3(c), and one can see the complex hysteretic relation (as shown in plot (a)) has been accurately represented. For the inverse hysteretic relation modeling, to achieve an efficient compensator with relatively sample construction, N_r and N_a were predefined as 8 and 7 with trials. After optimization, 16 operators and a 3^{rd}-order polynomial function were determined as shown in Fig. 3(d). It is noted that the given inverse hysteretic relation (as shown in the plot (b)) can be accurately captured by the simple model (2).

By using the static hysteresis inverse (2) as the compensator to compensate the static hysteresis shown in Fig. 3(a) (formula (2) of [34]), when applied the data shown in Fig. 3(e) as the desired signal and calculated with (2), the compensation relation can be achieved as shown in Fig. 3(f), where one can see the complex hysteresis can be effectively attenuated (with $\pm 2\%$ working range error) by using the relatively sample EUPI inverse.

B. Dynamic part compensator design

The linear dynamic portion is commonly represented in the transfer function form to facilitate frequency and uncertainty analysis. Dynamic portion of the SPM scanner provides frequency dependent properties which seriously influences dynamical reference tracking accuracy. Well compensation of dynamics will facilitate closed-loop controllers design, and will lead to faster convergence of control action. Generally, linear dynamics can be formatted in Laplace domain as $D_p(s)$ shown in (3),

$$D_p(s) = \frac{x_p(s)}{v(s)} = \frac{b_n s^n + \cdots + g_j s^j + \cdots + g_1 s + g_0}{s^n + \cdots + a_i s^i + \cdots + a_1 s + a_0}, \tag{3}$$

where $x_p(s)$ denotes the position output of the actuator; $v(s)$ stands for the input of dynamic component $D_p(s)$, and the output of the hysteretic portion, as well; $\{a_i \,|\, i \in \{1,\cdots,n\}\}$, $\{g_j \,|\, j \in \{1,\cdots,n\}\}$ with n representing the highest order, are associated parameters of the numerator and denominator, respectively.

To accurately model the dynamic portion of the SPM scanner, the established EUPI inverse should be implemented as a compensator to generate the drive signal for identification [34]. Since the EUPI inverse will well compensate the hysteretic portion as shown in Fig. 2, the rest input-output relation will be the pure dynamic part. Basically, since the dynamic portion may involve some unknown nonlinearity (represented as Δ), the achieved nominal model $D_p(s)$ will be an approximate input-output mapping.

To derive the dynamic inverse, representation (3) is transformed into (4),

$$D_p(s) = \frac{m_0(s+z_1)\cdots(s+z_i)}{(s+p_1)\cdots(s+p_i)} \cdot \frac{(s-z_{i+1})\cdots(s-z_n)}{(s+p_{i+1})\cdots(s+p_n)}, \tag{4}$$

where $z_1,\cdots,z_n$, $p_1,\cdots,p_n$ denote zeros and poles of the dynamic portion, m_0 is the associated gain, and n is the system's highest order.

This article has been accepted for publication in a future issue of this journal, but has not been fully edited. Content may change prior to final publication. Citation information: DOI 10.1109/TNANO.2018.2849404, IEEE Transactions on Nanotechnology

In this research, poles $p_1, \cdots, p_n$ are assumed to be positive, and zeros $z_1, \cdots, z_n$ are non-negative, based on the fact that input-output relations of most piezoelectric actuators are stable, but usually with non-minimum phase. It is noted that, the first term of (4) can be directly reversed to establish the inverse, however, the inverse of the second term is not realizable as there exist positive poles.

Fortunately, the scanning operation of an SPM is a spatial affair, time delay can be easily conquered by shifting data according to nominal phase response, and it will not influence the imaging process (spatial data collection). In other words, it needs only to maintain the output magnitude desirable. Based on this fact, the following inverse dynamic compensator $D_p^{-1}(s)$ is utilized,

$$\begin{aligned} D_p^{-1}(s) &= \frac{v(s)}{x_p^r(s)} \\ &= \frac{(s+p_1)\cdots(s+p_i)}{m_0(s+z_1)\cdots(s+z_i)} \cdot \frac{(s+p_{i+1})\cdots(s+p_n)}{(s+z_{i+1})\cdots(s+z_n)}. \end{aligned} \tag{5}$$

where $x_p^r(s)$ represents the reference input, and $v(s)$ denotes the output of the dynamic compensator. After compensating (4) using (5), the remaining dynamics becomes a time delay term, which will not influence the SPM scanning range. Based on the hysteresis inverse (2) and the dynamic inverse (5), the dynamic hysteresis compensator can be built as (6),

$$u(t) = H_p^{-1}[D_p^{-1}(s)x_p^r(t)], \tag{6}$$

and the associated schematic diagram can be found in Fig. 2 (b).

After cascading the dynamic hysteresis compensator (6) with the SPM scanner, the entire system can be generally represented as a virtual plant (7),

$$x(s) = (1+\Delta_L(s))x_p^r(s), \tag{7}$$

where $\Delta_L(s)$ denotes a bounded unknown portion represented in Laplace domain, which is with respect to the modeling uncertainty and the time delay terms. If the proposed composite inverse compensator (6) is accurate enough, $||\Delta_L(s)||_\infty$ will be much smaller than 1, with $||\cdot||_\infty$ representing the infinity norm. Under this condition, the composite compensator can be used to precisely regulate nanomanipulation systems without feedback.

To demonstrate the effectiveness of the proposed dynamic hysteresis compensator (6), simulation tests were conducted. During this test, static hysteresis data were first utilized to build the static hysteresis inverse (as shown in Fig. 3(b)), subsequently, pure dynamic data were extracted and identified as (8) (excited using a $0.01-30Hz$ chirp signal),

$$\begin{aligned} D_p(s) = &\frac{0.0099(s+501.9)(s+0.01816)}{(s+48.48)(s+0.01702)} \cdot \\ &\frac{(s-243.2+396.94j)(s-243.2-396.94j)}{(s+96.05+120.61j)(s+96.05-120.61j)}. \end{aligned} \tag{8}$$

One can see there are two zeros lying on the right half plane (RHP) of the complex domain, indicating the precise inverse dynamics is not realizable. Therefore, (5) is applied to build the composite compensator (6). After connecting compensator (6) to the built model consisting of hysteresis part (in Fig. 3(a)) and (8), its entire input-output relation can be found in Fig. 4(b), which is much better in contrast to that only uses static hysteresis compensator as illustrated in the plot (a) (tested using a $0.01-30Hz$ decaying chirp input signal).

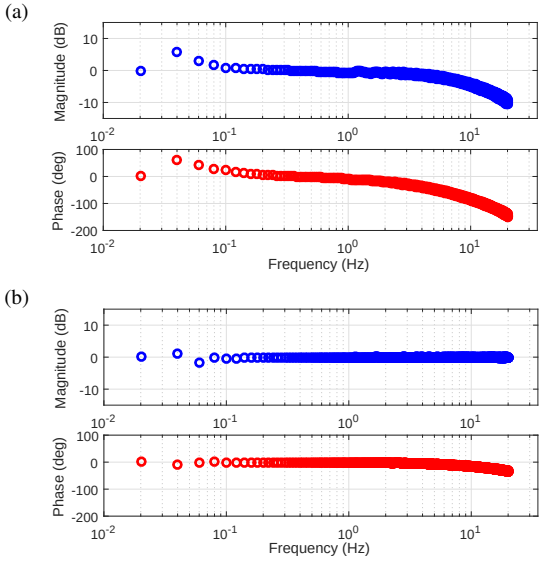

Fig. 4. Input-output relation of (a) virtual actuator with static hysteresis compensator, and (b) virtual actuator system with dynamic hysteresis compensator. Top panel: magnitude response, bottom panel: phase response.

Remark 1: This study employs the static EUPI inverse as part of the dynamic hysteresis compensator, since it is relatively simple and capable of representing various types of hysteresis precisely. In fact, other type hysteretic models can also be employed here, such as methods proposed in [26], [30], [32], [35], as far as they are precise enough, since large modeling error will generally lead to large system uncertainty, which may degrade ENVS controller's efficiency.

III. ENVS Controller Design and Analysis

NVS control method is actually a set based feedback approach, and it has been proposed for SPM motion control considering local feedback image as a set [15]. However, it is noted that the CNVS controller is prone to employ relatively large feedback image to guarantee full coverage of possible positioning error caused by uncertainty of the SPM actuator. The worse case is the CNVS approach may generate incorrect control signal under noisy situation. To solve these problems, the ENVS control strategy is developed in this section based on the derived linearized SPM virtual model of last section and a newly developed patch-based NVS approach.

The basic working principle of ENVS strategy is shown in Fig. 1. To feed back a local image, the SPM performs a local scan to probe a tiny area of interest. By doing this, an acceptable image feedback rate can be guaranteed [36]. During ENVS working, first, a large area of interest is scanned by SPM; then a small segment is chosen as the desired image (inside the large SPM image). Subsequently the tip starts the local scan to sample a current local image to feed back.

This article has been accepted for publication in a future issue of this journal, but has not been fully edited. Content may change prior to final publication. Citation information: DOI 10.1109/TNANO.2018.2849404, IEEE Transactions on Nanotechnology

According to these two sets corresponding to the desired image and current image, the ENVS controller calculates the moving direction and velocity for the SPM tip. ENVS controller keeps updating current local images until it matches the desired one. In this way, the tip can be steered to the goal location accurately.

In order to design such an ENVS control system, two fundamental issues should be solved: how to define a difference (distance) in NVS based on patch information, and how to derive a control law according to the set dynamics in the NVS.

A. Basic Concepts in ENVS Controller Design

Different from the set definition proposed for the CNVS [16], the set used in the ENVS is defined as follows: consider a $n \times n$ pixels image A, where $A = [a_{ij}], 1 \le i, j \le n$; for the same image A, its set form X is defined as (9):

$$\begin{cases} X = \{[1,1,I_{1,1}]^T, \cdots, [i,j,I_{i,j}]^T, \cdots, [n,n,I_{n,n}]^T\}, \\ I_{i,j} = [\{a_{k,l} : i - \dfrac{ls-1}{2} \le k \le i + \dfrac{ls-1}{2}, \\ \qquad j - \dfrac{ls-1}{2} \le l \le j + \dfrac{ls-1}{2}\}]^T \in \mathbb{R}^{(ls \times ls)}, \end{cases} \tag{9}$$

where ls, defined as an odd number, represents the patch size of each element of set form A; (i, j) denotes the patch location in pixel. Once k or l is less than 1, or k or l is greater than n, the associated intensity value $a_{k,l}$ of $I_{i,j}$ will be set to zero, which is an approach to tackle motion issue at boundary of the image A. It is noted that the basic elements of a set (local image) is actually a tiny image comprised of several pixels with center locating at (i, j). Since the basic element contains the center pixel and its neighbors, which provide sufficient location information compared to that of a single pixel element, therefore this method can attenuate the noise influence effectively, which is similar with the function of mean-value filter.

To determine whether two sets get matched, it has to evaluate the difference between two sets which work as the reference input and the system output regulated by the ENVS control scheme, respectively. In order to formulate the difference between two sets, the set distance should be defined. Any set distance $d(X,Y)$ between sets X and Y must satisfy three properties: symmetry, positive definiteness, and triangle inequality [37]. For instance, the Hausdorff distance is such an option [38], which has been successfully utilized in previous CNVS scheme, and it is also employed in this research to derive the ENVS control law.

Given a finite set of patches $X \subset \mathbb{P}$ ($\mathbb{P}$ represents the set $\{[i,\ j,\ I_{i,j}]^T \mid i,\ j \in Z^+\}$), the set distance between the set X and a patch $y \in \mathbb{P}$ is defined as following:

$$d_X(y) = \Big\{x : \min_{x \in X} \Big\{ \frac{||G(x-y)||}{||Gx||} \Big\}, x, y \in \mathbb{R}^{(ls \times ls+2)} \Big\}, \tag{10}$$

where $||\cdot||$ represents Euclidean norm; $G \in \mathbb{R}^{(ls \times ls+2) \times (ls \times ls+2)}$ denotes a diagonal weight matrix used to emphasize intensity information inside a patch (for instance, it is defined as $diag(g, g, 1, \cdots, 1)$, $g \in \mathbb{R}^+$ in this paper). The projection from y to X is denoted as $P_X(y) = \{x \in X : d_X(y)\}$. The Hausdorff distance between two sets X and Y can then be defined as:

$$\begin{aligned} \mathbb{D}(X,Y) = \max \big\{ & \max_{y \in Y} \{||y - P_X(y)|| \rho_Y(y)\}, \\ & \max_{x \in X} \{||x - P_Y(x)|| \rho_X(x)\} \big\}, \end{aligned} \tag{11}$$

where $0 \le \rho_X, \rho_Y \le 1$ denote probability functions defined for each element. Through using $\mathbb{D}(X,Y)$, one can analyze the convergence property of the ENVS control system.

To derive the ENVS control law, the next step is to introduce how a set evolves along time regulated by control signals. As a matter of fact, a set evolving with time is called a tube [38], denoted as $X(t)$. A tube $X(t) \subset \mathbb{P}$ is a mapping: $X : \mathbb{R}^+ \to \mathbb{P}$. An illustrative interpretation is that a sequence of surfaces, consisting of patches, evolve with respect to time in the three dimensional space.

To represent evolution of each patch inside the set X, a bounded Lipschitz function $\varphi : E \to \mathbb{P}$ with $E \subset \mathbb{P}$ is defined [38]. The set of all such functions is denoted as $\mathrm{BL}(E, \mathbb{P})$. Then, the transition of a set, with each patch evolving governed by the associated $\varphi \in \mathrm{BL}(E, \mathbb{P})$, can be defined as (12),

$$T_\varphi(t, X_0) = \{x(t) : \dot{x} = \varphi(x), x(0) \in X_0\}, \tag{12}$$

where $X_0 \subset \mathbb{P}$ represents the initial state of a tube $X(t)$ (or an original set), and $x(0) \in \mathbb{P}$ denotes a patch of $X(t)$ at the initial time. Then the semi-derivative of a tube $X(t)$, denoted as $\mathring{X}(t)$, can be defined as (13) based on mutation analysis [39],

$$\begin{aligned} \mathring{X}(t) = \big\{ & \varphi(x) \in \mathrm{BL}(E, \mathbb{P}) : \\ & \lim_{\Delta t \to 0^+} \frac{1}{\Delta t} \mathbb{D}(X(t+\Delta t), T_\varphi(\Delta t, X(t))) = 0 \big\}. \end{aligned} \tag{13}$$

Therefore, the set dynamics mutation equation can be defined as (14),

$$\varphi(x) \in \mathring{X}(t), \tag{14}$$

and the controllable mutation equation (let U be the set of all the possible control input $u(t)$) can be defined as:

$$\varphi(x(t), u(t)) \in \mathring{X}(t) \quad \text{with} \quad u(t) = \gamma(X(t)), \tag{15}$$

where $\varphi : E \times U \to \mathrm{BL}(E, \mathbb{P})$ is a mapping process from a state to a bounded Lipschitz function; $\gamma : \mathbb{P} \to U$ is a feedback mapping from an image $X(t)$ to the control input.

B. Analysis of Controllable Set Mutation for SPM based Nanomanipulation

The defined controllable set mutation (15) provides an alternative way to solve set matching problem via controlling its governing dynamics. In the generalized perspective, the patch dynamics $\dot{x} = \varphi(x)$ of $\mathring{X}(t)$ could be varying from one to other, which is hard to solve [40]. However, for specific tasks, such as control of the nanoscale motion actuated by SPM scanner with image feedback could be much easier [16]. This paper proposes to use the controllable set mutation (15) to describe the motion control issue of SPM scanners with image feedback in the NVS. As a matter of fact, each patch of an image set X can be represented utilizing a $ls \times ls + 2$ dimensional vector $x = [x_i, x_j, \mathrm{vect}(I_{i,j})]^T$ where x_i, x_j represent

This article has been accepted for publication in a future issue of this journal, but has not been fully edited. Content may change prior to final publication. Citation information: DOI 10.1109/TNANO.2018.2849404, IEEE Transactions on Nanotechnology

the horizontal and vertical coordinates of the patch center, which is governed by the scanner dynamics; $I_{i,j}$ is a $ls \times ls$ size tiny image consisting of samples height around the position specified by x_i, x_j; and vect$(\cdot)$ is a function to transform a matrix into the vector form.

In this ENVS controller design, as addressed in the section II, after dynamic hysteresis compensation, the entire SPM scanner input-output relation can be regarded as a virtual plant (7). Furthermore, an integral portion is cascaded to (7) to transform it into a new virtual plant with motion velocity as input (see Fig. 1), which is prevalent in macro-robot control. Under this case, SPM tips planar velocity will be able to be directly controlled to generate mutation of the set $X(t)$. The new virtual system's input $u_v(t)$ will have two translational components, which can be represented using $u_v(t) = [u_i(t), u_j(t)]^T$.

Consider images as patch-based sets, image evolutions, induced from the scanner motion, with respect to time comprise a tube. Therefore, the mutation of $X(t)$ will be derived from the input-output relation governing the previous built virtual system. It is noted that derivative $\dot{I}_{i,j}$ of the intensity part in $x(t)$ will be zero based on the fact that sample height at the same center point will be invariant within relatively long time. Since the velocity of the pixel in the image plane is opposite to the velocity of the SPM motion, consequently, the differential equation governing a patch evolution can be represented as (16),

$$\dot{x}(t) = B(I+\Delta_T)u_v(t), \quad B = \begin{bmatrix} -1 & 0 & 0 & \cdots & 0 \\ 0 & -1 & 0 & \cdots & 0 \end{bmatrix}^T, \quad (16)$$

where $\Delta_T \in R^{2\times 2}$ is the uncertainty matrix in diagonal form with respect to Δ_L of virtual system (7). Then each element of the controllable set mutation $\mathring{X}(t)$ can be represented as:

$$\varphi(x(t), u_v(t)) = B(I+\Delta_T)u_v(t) \in \mathring{X}(t), \quad (17)$$

which can be directly applied to control the evolution of an image sampled by SPM.

C. ENVS Controller Design for SPM based Nanomanipulation

With formulation of controllable set mutation, the stabilization problem of (17) can be defined as follows: design a controller: $u_v(t) = \gamma(X(t))$ (as mentioned in (15)) based on feedback set (current image) $X(t)$, so that $\mathbb{D}(X(t), \hat{X}) \to 0$ as $t \to \infty$, where $\hat{X}$ represents the desired image in its set form. To build such a control law $u_v(t)$ based on set feedback in the NVS, first a shape Lyapunov function is required, which should be a $\mathbb{P} \to \mathbb{R}^+$ function. Compared to the shape Lyapunov function defined in [38], this research proposes to use a more general and flexible shape Lyapunov function based on the introduced new Hausdorff distance $\mathbb{D}(\cdot)$ in (11), and its expression is:

$$\begin{aligned} V(X,t) = \frac{1}{2}\Big(& \int_X [(x - P_{\hat{X}}(x))^T \Lambda (x - P_{\hat{X}}(x)) \eta_X(x)] dx \\ & + \int_{\hat{X}} [(\hat{x} - P_X(\hat{x}))^T \Lambda (\hat{x} - P_X(\hat{x})) \eta_{\hat{X}}(\hat{x})] d\hat{x} \Big), \end{aligned} \quad (18)$$

where $\Lambda \in \mathbb{R}^{(ls\times ls+2)\times(ls\times ls+2)}$ is a diagonal weight matrix to emphasize position information inside a patch (for instance, it is defined as $(1+g)I - G$ in this paper); the probability function $\eta_Z(z)$ associated with $\rho_Z(z)$ in (11) is defined as:

$$\eta_Z(z) = \rho_Z^2(z) = \frac{\xi(z)}{\int_Z \xi(z) dz} \quad (19)$$

with $z \in Z$ and $Z = X$ or $\hat{X}$, to emphasize roles of different patches; $\xi(\cdot)$ of (19) has the following expression:

$$\begin{cases} \xi(x) = \exp\big(M \dfrac{(G(x - P_{\hat{X}}(x)))^T (G(x - P_{\hat{X}}(x)))}{(GP_{\hat{X}}(x))^T GP_{\hat{X}}(x)}\big), \\ \xi(\hat{x}) = \exp\big(M \dfrac{(G(\hat{x} - P_X(\hat{x})))^T (G(\hat{x} - P_X(\hat{x})))}{(G\hat{x})^T G\hat{x}}\big), \end{cases} \quad (20)$$

where G is the weight matrix defined in (10); $M \in \mathbb{R}^-$ is an adjustable negative gain to modify efficiency of weight function $\eta(\cdot)$.

With the newly defined shape Lyapunov function (18) in the NVS, the image (governed by controllable set mutation $\varphi(x(t), u_v(t)) \in \mathring{X}(t)$) based stabilizing controller $\gamma(X(t))$ can be formulated. For the special implementation of nanomanipulation system, the governing differential equation of a patch is defined as $x(t)$ independent linear equation (16). Thus for such a system, the stabilizing control law in the NVS can be designed according to the following theorem:

Theorem 1: For the system formulated in the NVS: $B(I+\Delta_T)u_v(t) \in \mathring{X}(t)$, with $u_v(t) \in \mathbb{R}^2$, $B \in \mathbb{R}^{(ls\times ls+2)\times 2}$, $X(t) \subset \mathbb{P}$, $X(0) = X_0$, and the upper boundary of uncertainty $||\Delta_T||_\infty < 1$, the following control law (named ENVS control law) can stabilize it at a given desired set $\hat{X}$ in the neighborhood of X_0:

$$u_v(t) = -\alpha E(X,t), \quad (21)$$

where $\alpha \in \mathbb{R}^+$ is a design gain to regulate the convergence rate, and $E(X,t) \in \mathbb{R}^2$ is a column vector defined as:

$$\begin{aligned} & E(X,t) = \\ & \quad B^T \Big\{ \int_X \Big[\Lambda(x - P_{\hat{X}}(x)) \eta(x) \\ & - \frac{1}{2}(\zeta(x) - \frac{\int_X \xi'(x)dx}{\int_X \xi(x)dx})(x - P_{\hat{X}}(x))^T \Lambda(x - P_{\hat{X}}(x)) \eta(x) \Big] dx \Big\} \\ & - B^T \Big\{ \int_{\hat{X}} \Big[\Lambda(\hat{x} - P_X(\hat{x})) \eta(\hat{x}) \\ & - \frac{1}{2}(\zeta(\hat{x}) - \frac{\int_{\hat{X}} \xi'(\hat{x})dx}{\int_{\hat{X}} \xi(\hat{x})dx})(\hat{x} - P_X(\hat{x}))^T \Lambda(\hat{x} - P_X(\hat{x})) \eta(\hat{x}) \Big] d\hat{x} \Big\} \end{aligned} \quad (22)$$

with $\xi'(\cdot) = \zeta(\cdot)\xi(\cdot)$ denoting the derivative of $\xi(\cdot)$ with respect to the variable x^T.

Proof 1: When the set mutation $B(I+\Delta_T)u_v(t) \in \mathring{X}(t)$ is employed, the mutation of shape Lyapunov function $V(X,t)$

This article has been accepted for publication in a future issue of this journal, but has not been fully edited. Content may change prior to final publication. Citation information: DOI 10.1109/TNANO.2018.2849404, IEEE Transactions on Nanotechnology

(18) with respect to time can be derived as:

$$\begin{aligned}
&\mathring{V}(X,t) = \\
&\quad u_v^T(t)B^T(I+\Delta_T)\Bigg\{\int_X \Big[\Lambda(x-P_{\hat{X}}(x))\eta(x) \\
&-\frac{1}{2}(\zeta(x)-\frac{\int_X \xi'(x)dx}{\int_X \xi(x)dx})(x-P_{\hat{X}}(x))^T\Lambda(x-P_{\hat{X}}(x))\eta(x)\Big]dx\Bigg\} \\
&-u_v^T(t)B^T(I+\Delta_T)\Bigg\{\int_{\hat{X}} \Big[\Lambda(\hat{x}-P_X(\hat{x}))\eta(\hat{x}) \\
&-\frac{1}{2}(\zeta(\hat{x})-\frac{\int_{\hat{X}} \xi'(\hat{x})dx}{\int_{\hat{X}} \xi(\hat{x})dx})(\hat{x}-P_X(\hat{x}))^T\Lambda(\hat{x}-P_X(\hat{x}))\eta(\hat{x})\Big]d\hat{x}\Bigg\} \\
&= u_v^T(t)(I+\Delta_T)E(X,t).
\end{aligned} \tag{23}$$

When the ENVS control law (21) is applied, $\mathring{V}(X,t)$ will be equal to $-\alpha(I+\Delta_T)E^T(X,t)E(X,t)$, which will always be non-positive under the condition $||\Delta_T||_\infty < 1$. Therefore, convergence of the set tracking problem in the CNVS can be guaranteed by the proposed ENVS control law $u_v(t)$.

D. Discussion

It is noted that *Theorem 1* requires the uncertainty Δ_T to be "small" to derive the stabilizing ENVS control law. Previous works such as [15], [16], didn't take it into consideration. Therefore, the derived CNVS controllers may diverge under some situations. To solve this problem under CNVS scheme, it requires either a larger local image or a sequence of smaller images, both of which will lead to a higher computational cost. This work filled in the gap of previous studies by introducing the dynamic hysteresis compensator (6) to linearize input-output relation of SPM actuators.

Theorem 1 only addresses the neighborhood stabilization problem. In fact, the ENVS control scheme (as shown in Fig. 1) can realize large scale positioning accurately. This is because, via assistance of the dynamic compensator (6), the SPM tip can reach any location's neighborhood uniformly, which can geometrically explained as a circle area with the desired position as its circle center and the uncertainty $C_0||\Delta_T||_\infty$ as its radius (where C_0 is a constant); then the control law $u_v(t)$ can be applied to reduce the feedforward SPM tip control error using a smaller feedback image. Based on this strategy, this ENVS controller enables the SPM tip to "jump" in the NVS.

The ENVS control scheme employs the patch $x(t)$ elements as well as the weighted shape Lyapunov function (18) to effectively determine the moving direction and velocity. However, it should be pointed that, the computational cost of the ENVS is much larger than that of CNVS under same feedback set size, which is a tradeoff between the robustness and efficiency. On behalf of the compensation effect by (6), which effectively attenuates system uncertainty, the ENVS scheme is capable of employing much smaller feedback set compared to that of CNVS, thus reduces the computational cost.

Regarding efficiency, it should also be pointed out that, for the entire ENVS or CNVS control scheme, the most time consuming part is the feedback data collection procedure, which utilizes physical system to conduct scanning motion. Therefore, in real implementation, the control scheme that uses smaller feedback set will suffer less time cost, and thus the proposed ENVS control scheme can be executed more efficiently than the CNVS scheme.

IV. Demonstration of ENVS Controller on AFM based Nanomanipulation System

To demonstrate performance of the proposed ENVS control scheme under various conditions, simulation studies based on the normalized hysteresis model shown in Fig. 2(a) and the linear dynamics (8) were conducted.

A. Setup of the Simulation Platform

Based on the established dynamic hysteresis model of the general AFM scanner, the dynamic hysteresis compensator was built (in the section II) to attenuate the unwanted input-output relation to facilitate patch-based NVS part design. To test the effectiveness of the proposed ENVS control scheme, a CNVS controller with complete image feedback proposed in [16] was employed as the contrast. To conduct comparable tests, the CNVS controller is also equipped with the same dynamic hysteresis compensator. Comparative tests between the ENVS and CNVS approaches were conducted on a virtual AFM platform [41] with DNA sample (as shown in Fig. 5), to freely evaluate the tip positioning and tracking performance under scenarios with imaging noise, drift and tilt.

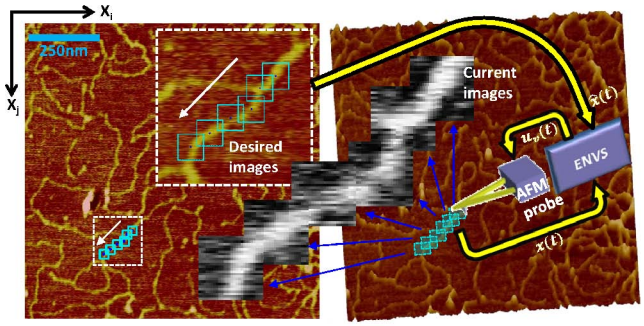

Fig. 5. AFM scanned DNA sample image (1024×1024 pixels) for testing.

During the tests, the size for local scan image was set to 31×31 pixels, which could be effectively sampled during practical implementation [15]. At beginning of the tests, the tip of AFM was assumed to locate at the center of the image, which is a normal case for the AFM based nanomanipulator [33]; then we selected an local scan image of interest as the desired image; then the desired image's indexes (x_i, x_j) at image center were directly sent to the composite compensation part (as shown in Fig. 1), and subsequently the tip was driven to the neighbourhood of (x_i, x_j); after several milliseconds, the CNVS or the ENVS control part started to work, this is how the EVNS controller enable the AFM tip to "jump" in the NVS control scheme.

B. Setpoint Control Comparison between CNVS and ENVS

To fully test positioning performances of CNVS and ENVS controller, a sufficient drift was added to disturb the system,

This article has been accepted for publication in a future issue of this journal, but has not been fully edited. Content may change prior to final publication. Citation information: DOI 10.1109/TNANO.2018.2849404, IEEE Transactions on Nanotechnology

which was represented as an offset ($d_n(t)$ in Fig. 2(a)) for the image tracking. As an instance, for this test, the offset was set to $(17,-17)$ pixels for the selected desired location $(x_i,x_j) = (718,374)$. During the tests, a considerably large noise (10% of local height in this study, based on combined factors comprised of improper tip-sample interaction, laser noise, sampling and control noise introduced by customer developed system) was also added to the scanning operation to simulate the measurement uncertainty of local surface height. As an instance, here we added a random noise (proportional to the local pixel height value) to the original value at each pixel. As a common case, tilt sample introduces slope to feedback image, which may affect performance of the NVS method. As an instance, the slope $S_{X_i} = 1.0$ and $S_{X_j} = 0.7$ along X_i, X_j axis respectively, were involved in the test to mimic the tilt sample scenario.

After simulated using Matlab *m*-script, the following results were obtained. Fig. 6 shows the CNVS test without noise. The plot (a), (c) illustrate that the current image via local scan converged to the desired one smoothly, and the shape Lyapunov function converged exponentially fast (Fig. 6(b)) [39]. It is noted that, the shape Lyapunov function value shown in Fig. 6(b) is not very consistent with the positioning error shown in (c), which is because the shape Lyapunov function considers both image intensity error and the positioning error, therefore it may not be very consistent to the positioning error shown in Fig. 6(c).

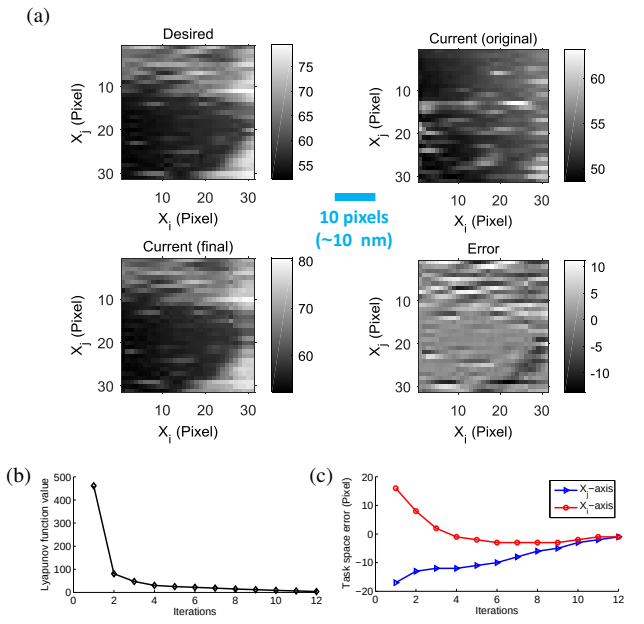

Fig. 6. CNVS controller (with dynamic hysteresis compensator) testing under noise-free case, (a) desired image tracking results, (b) convergence of shape Lyapunov function [16], (c) positioning errors along X_i, X_j axis in pixel.

When the random noise (10% sampled local height) was added to the original current image at each pixel, after testing, the results are shown in Fig. 7. The plot (a), (c) illustrate the AFM tip went to a wrong location, though the shape Lyapunov function converged exponentially fast (as shown in Fig. 7(b)) [39]. This is caused by the heavy noise, which challenges the conventional pixel-wise-based set distance calculation method.

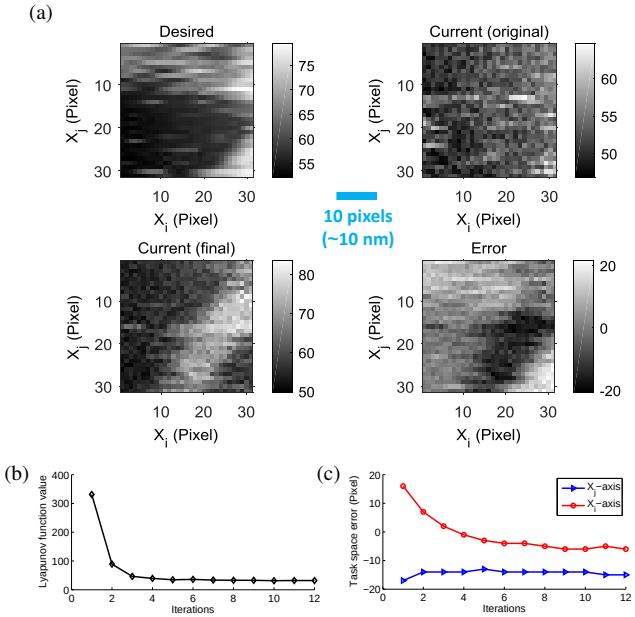

Fig. 7. CNVS controller (with dynamic hysteresis compensator) testing with heavy noise, (a) desired image tracking results, (b) convergence of shape Lyapunov function [16], (c) positioning errors along X_i, X_j axis in pixel.

The proposed ENVS controller was tested under the noise condition and the testing results are shown in Fig. 8, where 11×11-pixel-patch information was employed. From Fig. 8(a), one can see though the current image sampled by local scan was considerably noisy, the high positioning precision shown in Fig. 8(c) was obtained by the ENVS strategy. It is noted that, the shape Lyapunov function value shown in Fig. 8(b) is more consistent with the positioning error (Fig. 8(c)) compared with the CNVS case, this is because the shape Lyapunov function is capable of emphasizing image content error and the positioning error separately through weight matrix G and Λ.

C. Sequence and Stochastic Positioning Control Tests

For potential tasks such as genome sequencing, the SPM tip is usually required to firmly follow the DNA strip. Therefore, the strip tracking test was conducted for demonstrating capability of the ENVS control scheme. During testing, 6 locations of a DNA strip shown in Fig. 5 were selected as the desired image sequence. At each location, 5 iterations were set for the ENVS controller to converge. The testing condition was assumed to be the same as previous testing: 10% noise, $(17,-17)$ drift and $S_{X_i} = 1.0$, $S_{X_j} = 0.7$ for the slope. The testing result is shown in Fig. 9, from the plot (a) one can see current images at different locations can gradually converge to the desired ones even with substantial noise. Fig. 9(b) shows the shape Lyapunov function converges exponentially fast at each location. The associated 2D positioning errors are illustrated in Fig. 9(c). It can be found the maximum steady state error is 1 pixel off the desired location (in horizontal and vertical directions) at the testing condition, which indicates positioning error of the ENVS method is generally bounded by $2/1024 \approx 0.2\%$ of the tracking task with aforementioned testing condition.

This article has been accepted for publication in a future issue of this journal, but has not been fully edited. Content may change prior to final publication. Citation information: DOI 10.1109/TNANO.2018.2849404, IEEE Transactions on Nanotechnology

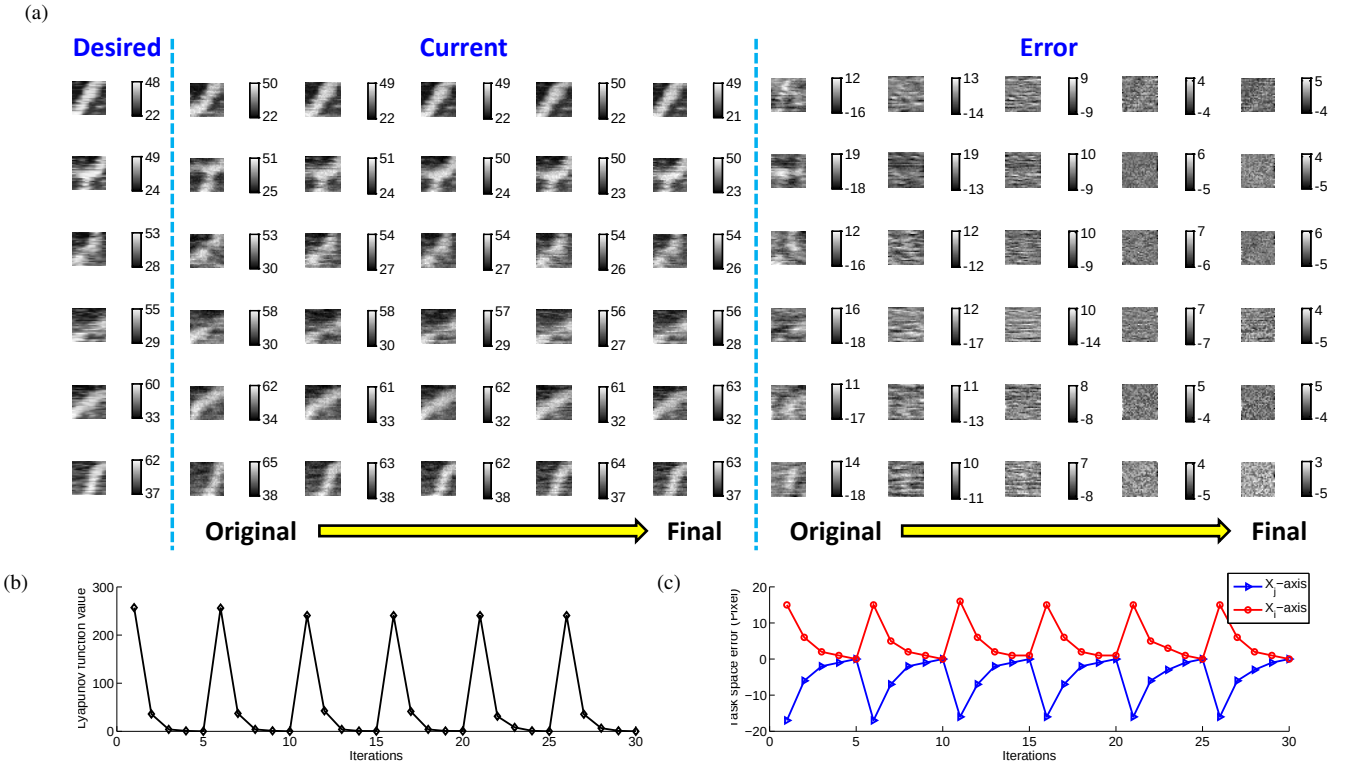

Fig. 9. DNA sequence tracking testing with ENVS controller, (a) illustration of images tracking results, (b) convergence of shape Lyapunov function (18) at each location, (c) positioning errors along X_i, X_j axis in pixel.

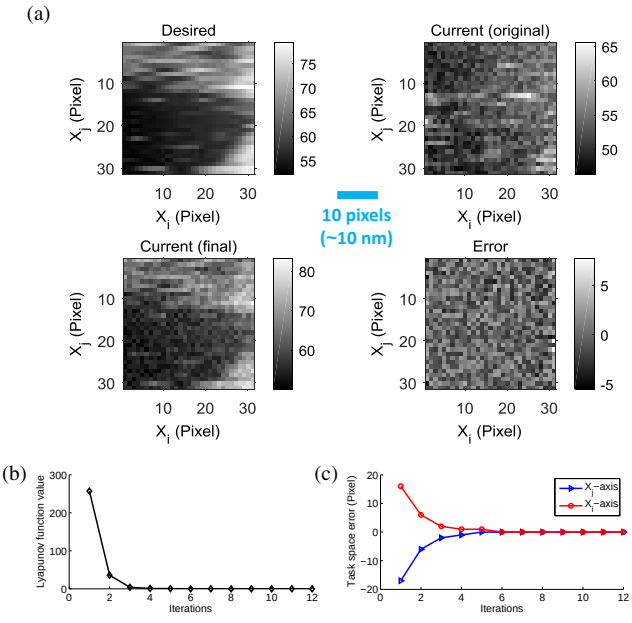

Fig. 8. ENVS controller test results, (a) desired image tracking results, (b) convergence of shape Lyapunov function (18), (c) positioning errors along X_i, X_j axis in pixel.

To further demonstrate repeatability of the ENVS control accuracy, stochastic positioning test was carried out. During this test, 100 desired locations were randomly selected within the DNA image (as shown in Fig. 10(a)), leaving 5% area for the margin. 8 iterations were set to the ENVS controller (different from the sequence tracking test (5 iterations)) to allow adequate time for control error convergence at most locations. The test has been repeated for 5 times, and the statistical results are illustrated in Fig. 10(b) and (c), where no-error-case (calculated in pixel) is $95.2 \pm 2.2\%$ for the X_i direction, and $88.2 \pm 1.3\%$ for the X_j direction, respectively. When it comes to the 1-pixel-error-case, it becomes $3.6 \pm 2.0\%$ for the X_i direction, and $10.8 \pm 1.4\%$ for the X_j direction, respectively. It is noted that probability of the within-1-pixel-error (0.2% of working range) results reaches more than 98%, while we also need to explain that, the outside-1-pixel-error cases are mostly caused by slow convergence rate, attributing to the combined effects induced by the added noise and the uncompensated hysteresis shown in Fig. 3(f).

Through these tests, the effectiveness of the ENVS control method is verified.

V. Conclusions

NVS control method provides a good performance (accuracy) in motion control that enables SPM to conduct more delicate nanomanipulations. In this study, the ENVS control scheme is proposed for guiding SPM based nanomanipulaton. This study is an extension to our previous works of proposed CNVS controller, which includes two brand new techniques: dynamic hysteresis compensator design approach and the patch-based NVS control method, enable the regulated SPM tip to "jump" and to reject heavy noise and drift during operation, which are urgent needed for practical implementation. Additionally, the ENVS control technique is easy to implement in any kind of SPMs to realize precise motion control for nanomanipulation in physical and biomedical study.

This article has been accepted for publication in a future issue of this journal, but has not been fully edited. Content may change prior to final publication. Citation information: DOI 10.1109/TNANO.2018.2849404, IEEE Transactions on Nanotechnology

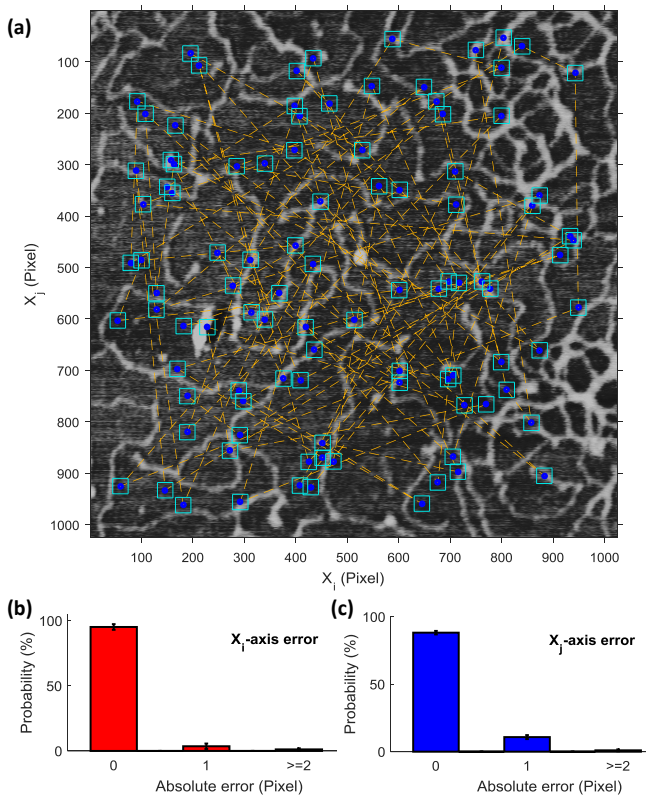

Fig. 10. Stochastic tracking test with ENVS controller, (a) randomly generated desired local images, (b) mean value and variance of X_i axis tracking error, (c) probability of X_j axis tracking error.

VI. Acknowledgements

The authors would like to thank Dr. Chanmin Su of the Bruker Nano Surface Instrumentation Group for his technical advice and help during the process of this research. Bo Song would also like to thank the support of the Recruitment Program of Global Experts for Young Professionals. Liangliang Chen would also like to thank Shenzhen Peacock Plan (KQTD 2016053114423644) and NSFC (U1613214) for partial support.

References

[1] C. Mavroidis and A. Ferreira, *Nanorobotics: current approaches and techniques*. Springer Science & Business Media, 2013.

[2] S. Kim, F. Shafiei, D. Ratchford, and X. Li, "Controlled afm manipulation of small nanoparticles and assembly of hybrid nanostructures," *Nanotechnology*, vol. 22, no. 11, p. 115301, 2011.

[3] H. Xie and S. Régnier, "High-efficiency automated nanomanipulation with parallel imaging/manipulation force microscopy," *IEEE Transactions on Nanotechnology*, vol. 11, no. 1, pp. 21–33, 2012.

[4] Y. Shen, M. Nakajima, Z. Zhang, and T. Fukuda, "Dynamic force characterization microscopy based on integrated nanorobotic afm and sem system for detachment process study," *IEEE/ASME Transactions on Mechatronics*, vol. 20, no. 6, pp. 3009–3017, 2015.

[5] P. Zhou, H. Yu, J. Shi, N. Jiao, Z. Wang, Y. Wang, and L. Liu, "A rapid and automated relocation method of an afm probe for high-resolution imaging," *Nanotechnology*, vol. 27, no. 39, p. 395705, 2016.

[6] R. Yang, B. Song, Z. Sun, K. W. C. Lai, C. K. M. Fung, K. C. Patterson, K. Seiffert-Sinha, A. A. Sinha, and N. Xi, "Cellular level robotic surgery: Nanodissection of intermediate filaments in live keratinocytes," *Nanomedicine: Nanotechnology, Biology and Medicine*, vol. 11, no. 1, pp. 137–145, 2015.

[7] L. Dong, K. Shou, D. R. Frutiger, A. Subramanian, L. Zhang, B. J. Nelson, X. Tao, and X. Zhang, "Engineering multiwalled carbon nanotubes inside a transmission electron microscope using nanorobotic manipulation," *IEEE Transactions on Nanotechnology*, vol. 7, no. 4, pp. 508–517, 2008.

[8] T. Ando, T. Uchihashi, and N. Kodera, "High-speed afm and applications to biomolecular systems," *Annual Review of Biophysics*, vol. 42, pp. 393–414, 2013.

[9] G. Li, N. Xi, M. Yu, and W.-K. Fung, "Development of augmented reality system for afm-based nanomanipulation," *IEEE/ASME Transactions on Mechatronics*, vol. 4, no. 9, pp. 358–365, 2004.

[10] R. V. Lapshin, "Automatic drift elimination in probe microscope images based on techniques of counter-scanning and topography feature recognition," *Measurement Science and Technology*, vol. 18, no. 3, pp. 907–927, 2007.

[11] B. Mokaberi and A. A. G. Requicha, "Compensation of scanner creep and hysteresis for AFM nanomanipulation," *IEEE Transactions on Automation Science and Engineering*, vol. 5, no. 2, pp. 197–206, 2008.

[12] Y. Zhang, Y. Fang, X. Zhou, and X. Dong, "Image-based hysteresis modeling and compensation for an afm piezo-scanner," *Asian Journal of Control*, vol. 11, no. 2, pp. 166–174, 2009.

[13] G. Li, Y. Wang, and L. Liu, "Drift compensation in afm-based nanomanipulation by strategic local scan," *IEEE Transactions on Automation Science and Engineering*, vol. 9, no. 4, pp. 755–762, 2012.

[14] M. Rana, H. R. Pota, and I. R. Petersen, "Improvement in the imaging performance of atomic force microscopy: A survey," *IEEE Transactions on Automation Science and Engineering*, vol. 14, no. 2, pp. 1265–1285, 2017.

[15] B. Song, J. Zhao, N. Xi, H. Chen, K. W. C. Lai, R. Yang, and L. Chen, "Compressive feedback-based motion control for nanomanipulationłtheory and applications," *IEEE Transactions on Robotics*, vol. 30, no. 1, pp. 103–114, 2014.

[16] J. Zhao, B. Song, N. Xi, L. Sun, H. Chen, and Y. Jia, "Non-vector space approach for nanoscale motion control," *Automatica*, vol. 50, no. 7, pp. 1835–1842, 2014.

[17] Z. Liu, J. Wang, and K. Poh, "Set-based modeling and observer design for planar structure from motion," *IEEE Transactions on Aerospace and Electronic Systems*, vol. 52, no. 3, pp. 990–1005, 2016.

[18] C. Liu, R. Chen, J. Xu, J. Zhao, H. Chen, N. Xi, and K. Chen, "Set space visual servoing of a 6-dof manipulator," in *Robotics and Automation (ICRA)*. IEEE, 2017, pp. 4422–4428.

[19] A. J. Fleming, "Nanopositioning system with force feedback for high-performance tracking and vibration control," *IEEE/ASME Transactions on Mechatronics*, vol. 15, no. 3, pp. 433–447, 2010.

[20] H. Habibullah, H. R. Pota, I. R. Petersen, and M. Rana, "Tracking of triangular reference signals using lqg controllers for lateral positioning of an afm scanner stage," *IEEE/ASME Transactions on Mechatronics*, vol. 19, no. 4, pp. 1105–1114, 2014.

[21] G.-Y. Gu, C.-X. Li, L.-M. Zhu, and C.-Y. Su, "Modeling and identification of piezoelectric-actuated stages cascading hysteresis nonlinearity with linear dynamics," *IEEE/ASME Transactions on Mechatronics*, vol. 21, no. 3, pp. 1792–1797, 2016.

[22] Z. Li, X. Zhang, G.-Y. Gu, X. Chen, and C.-Y. Su, "A comprehensive dynamic model for magnetostrictive actuators considering different input frequencies with mechanical loads," *IEEE Transactions on Industrial Informatics*, vol. 12, no. 3, pp. 980–990, 2016.

[23] K. K. Leang, Q. Zou, and S. Devasia, "Feedforward control of piezoactuators in atomic force microscope systems," *Control Systems, IEEE*, vol. 29, no. 1, pp. 70–82, 2009.

[24] P. Ge and M. Jouaneh, "Tracking control of a piezoceramic actuator," *IEEE Transactions on Control Systems Technology*, vol. 4, no. 3, pp. 209–216, 1996.

[25] P. Krejci and K. Kuhnen, "Inverse control of systems with hysteresis and creep," *IEE Proceedings-Control Theory and Applications*, vol. 148, no. 3, pp. 185–192, 2001.

[26] K. Kuhnen, "Modeling, identification and compensation of complex hysteretic nonlinearities: A modified prandtl-ishlinskii approach," *European Journal of Control*, vol. 9, no. 4, pp. 407–418, 2003.

[27] M. A. Janaideh, J. Mao, S. Rakheja, W. Xie, and C.-Y. Su, "Generalized prandtl-ishlinskii hysteresis model: Hysteresis modeling and its inverse for compensation in smart actuators," in *47th IEEE Conference on Decision and Control*, 2008, pp. 5182–5187.

[28] D. Davino, A. Giustiniani, and C. Visone, "Fast inverse preisach models in algorithms for static and quasistatic magnetic-field computations," *IEEE Transactions on Magnetics*, vol. 44, no. 6, pp. 862–865, 2008.

[29] J. Zhang, E. Merced, N. Sepúlveda, and X. Tan, "Modeling and inverse compensation of nonmonotonic hysteresis in vo-coated microactuators,"

IEEE/ASME Transactions on Mechatronics, vol. 19, no. 2, pp. 579–588, 2014.

[30] Z. Sun, N. Xi, Y. Cheng, S. Bi, C. Li, and L. Chen, "Exact inversion of discrete preisach model for compensating complex hysteresis in afm based nanomanipulator," in *International Conference on Nanotechnology (IEEE-NANO)*. IEEE, 2017, pp. 430–433.

[31] Z. Li, C.-Y. Su, and T. Chai, "Compensation of hysteresis nonlinearity in magnetostrictive actuators with inverse multiplicative structure for preisach model," *IEEE Transactions on Automation Science and Engineering*, vol. 11, no. 2, pp. 613–619, 2014.

[32] M. Al Janaideh, S. Rakheja, and C.-Y. Su, "An analytical generalized prandtl–ishlinskii model inversion for hysteresis compensation in micropositioning control," *IEEE/ASME Transactions on Mechatronics*, vol. 16, no. 4, pp. 734–744, 2011.

[33] Z. Sun, B. Song, N. Xi, R. Yang, L. Hao, Y. Yang, and L. Chen, "Asymmetric hysteresis modeling and compensation approach for nanomanipulation system motion control considering working-range effect," *IEEE Transactions on Industrial Electronics*, vol. 64, no. 7, p. 5513, 2017.

[34] Z. Sun, L. Hao, B. Song, R. Yang, R. Cao, and Y. Cheng, "Periodic reference tracking control approach for smart material actuators with complex hysteretic characteristics," *Smart Materials and Structures*, vol. 25, no. 10, p. 105029, 2016.

[35] Z. Li, J. Shan, and U. Gabbert, "Inverse compensation of hysteresis using krasnoselskii-pokrovskii model," *IEEE/ASME Transactions on Mechatronics*, 2018.

[36] L. Liu, Y. Luo, N. Xi, Y. Wang, J. Zhang, and G. Li, "Sensor referenced real-time videolization of atomic force microscopy for nanomanipulations," *IEEE/ASME Transactions on Mechatronics*, vol. 13, no. 1, pp. 76–85, 2008.

[37] W. Rudin, *Principles of Mathematical Analysis, Third Edition*. New York City, U.S: McGraw-Hill Science/Engineering/Math, 1976.

[38] L. Doyen, "Shape laypunov functions and stabilization of reachable tubes of control problems," *Journal of Mathematical Analysis and Applications*, vol. 184, no. 2, pp. 222–228, 1994.

[39] ——, "Mutational equations for shapes and vision-based control," *Journal of Mathematical Imaging and Vision*, vol. 5, no. 2, pp. 99–109, 1995.

[40] H. Huang, J. Zhao, and N. Xi, "Featureless visual tracking based on non-vector space control theory," *IFAC Proceedings*, vol. 47, no. 3, pp. 7318–7323, 2014.

[41] Z. Sun, B. Song, N. Xi, R. Yang, L. Chen, Y. Cheng, S. Bi, C. Li, and L. Hao, "Systematic hysteresis compensator design based on extended unparallel prandtl-ishlinskii model for spm imaging rectification," *IFAC Proceedings*, vol. 50, no. 1, pp. 10 901–10 906, 2017.

Bo Song (M'16) received the Ph.D. degree in electrical engineering from Michigan State University, East Lansing, MI, USA in 2016.

He is currently working as a Professor at the Lab of Robot Sensor Robot & Human-Machine Interaction, Institute of Intelligent Machines, Chinese Academic of Science, Hefei, China. His research interests include micro/nanorobotics and systems, micro/nanomanufacturing, nanomechanics, biomechanics, imaging and characterization in nanoscale, and compressive sensing and control with limited information.

Zhiyong Sun (M'16) received the Ph.D. degree in mechatronics engineering from Northeastern University, Shenyang, China in 2016.

He is currently a Post-doctoral Fellow with the Department of Industrial and Manufacturing Systems Engineering at the University of Hong Kong, Hong Kong, China. His research interests include micro/nanorobotics, bioMEMS, and modeling/control of smart material sensors and actuators.

Ning Xi (F'07) received the D.Sc. degree in systems science and mathematics from Washington University, St. Louis, Missouri, USA in 1993.

He is currently the Chair Professor of Robotics and Automation in the Department of Industrial and Manufacturing Systems Engineering, and the Director of Emerging Technologies Institute at the University of Hong Kong. Prof. Xi was a former Distinguished Professor and John D. Ryder Professor of Electrical and Computer Engineering with Michigan State University, East Lansing, MI, USA. He is a fellow of IEEE and he also served as the President of IEEE Nanotechnology Council (2010-2011). His research interests include robotics, manufacturing automation, micro/nano manufacturing, nano sensors and devices, and intelligent control and systems.

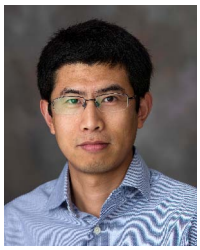

Ruiguo Yang (M'14) received the Ph.D. degree in electrical and computer engineering from Michigan State University, East Lansing, MI, USA in 2014.

He is currently an Assistant Professor in the Department of Mechanical and Materials Engineering at University of Nebraska-Lincoln, Lincoln, NE, USA. His main research interests include micro/nanorobotics, micro/nanomanipulation, bioMEMS and mechanobiology.

Yu Cheng (S'10) is currently a Ph.D. candidate in the Department of Electrical and Computer Engineering at Michigan State University, MI, USA.

His research interests include human-machine interaction, tactile sensing, and robot modeling and control.

Liangliang Chen received the Ph.D. degree in electrical and computer engineering from Michigan State University, East Lansing, MI, USA in 2015.

He is currently working at Shenzhen Academy of Robotics. His research interests include ultra weak signal detection in nano sensors, signal processing, analog circuits, CNT nanosensors, biosensor and medical imaging enhancement.

Lixin Dong (SM'10) received the Ph.D. degree in microsystems engineering from Nagoya University, Nagoya, Japan, in 2003.

He is currently an Associated Professor in the Department of Electrical and Computer Engineering at Michigan State University, East Lansing, MI, USA. Dr. Dong received the National Science Foundation Career Award in 2011, the 2008 American Publishers Awards for Professional and Scholarly Excellence, and the IEEE Transactions on Automation Science and Engineering Googol Best New Application Paper Award in 2007. His research interests include nanorobotics, nanoelectromechnical systems, mechatronics, mechanochemistry, and nanobiomedical devices.